Electronic Supplementary Information (ESI)

Space Charge Enhanced Ion Transport in Heterogeneous Polyelectrolyte/Alumina Nanochannel Membranes for High-Performance Osmotic Energy Conversion

Chen-Wei Chang,[1,+] Chien-Wei Chu,[1,+] Yen-Shao Su,[1,+] Li-Hsien Yeh,[1,*]

[1]Department of Chemical Engineering, National Taiwan University of Science and Technology, Taipei 10607, Taiwan

* Corresponding Author:

Li-Hsien Yeh (Email: lhyeh@mail.ntust.edu.tw, TEL: +886-2-27376942);

+ These authors contributed equally to this work

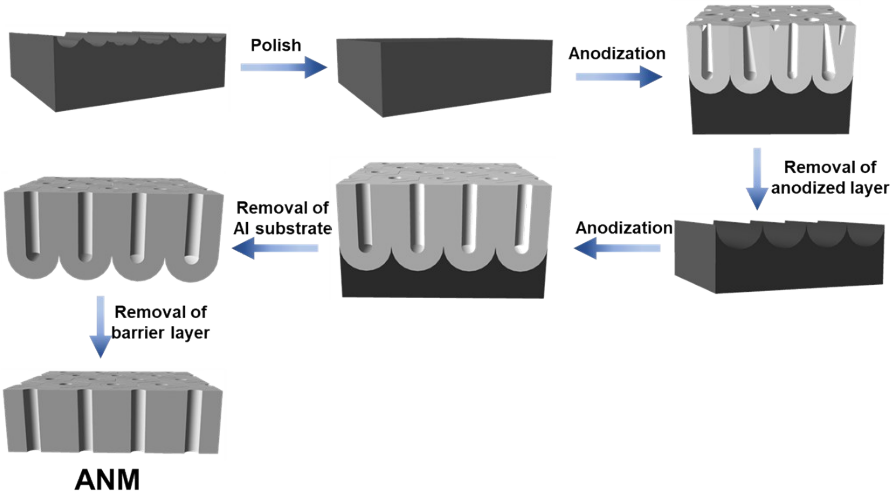

Fig. S1. Schematic illustration of the two-step anodization procedure we employed for the fabrication of alumina nanochannel membrane (ANM) with highly ordered straight channels.

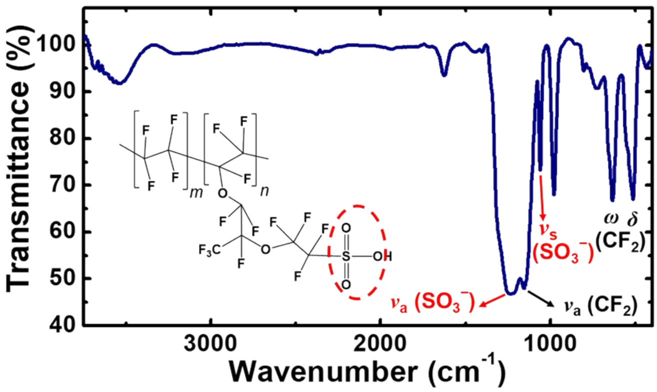

Fig. S2. FTIR spectrum of Nafion. The ν_a and ν_s marked in red are assigned to the asymmetric and symmetric stretching vibrations of the sulfonate groups ($-SO_3^-$), respectively. The ν_a marked in black, ω, and δ are assigned to F−C−F vibrations of the asymmetric stretching, the out-of-plane wagging, and the in-plane scissoring modes, respectively.

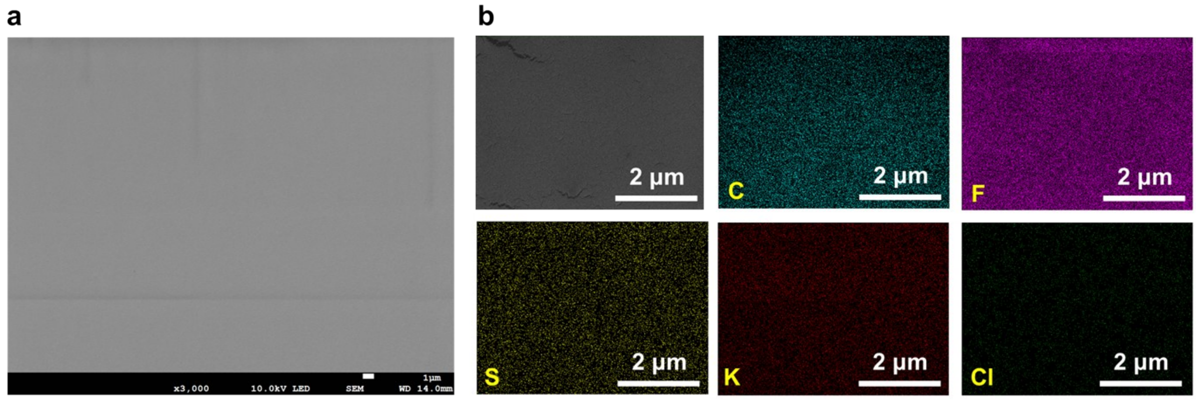

Fig. S3. (a) SEM image of the top Nafion layer on a large scale. (b) SEM and EDX elemental mapping characterizations of the Nafion film on a local scale. The images were captured after immersing the membrane in 1 M KCl solution for 30 min. The signal intensity of potassium (red) is apparently stronger than that of chlorine (green), suggesting strong cation-selectivity of Nafion.

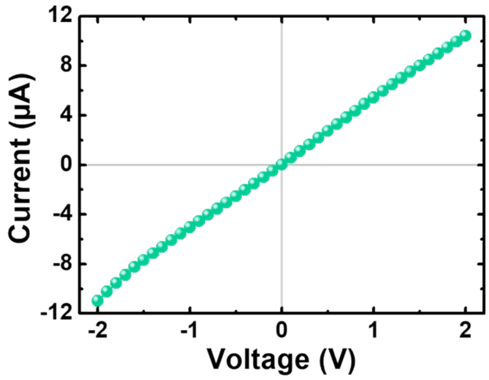

Fig. S4. I-V characteristic of the pure Nafion membrane in 10 mM KCl solution. The linear I-V relationship indicates non-rectifying feature of the homogeneous Nafion polyelectrolyte membrane.

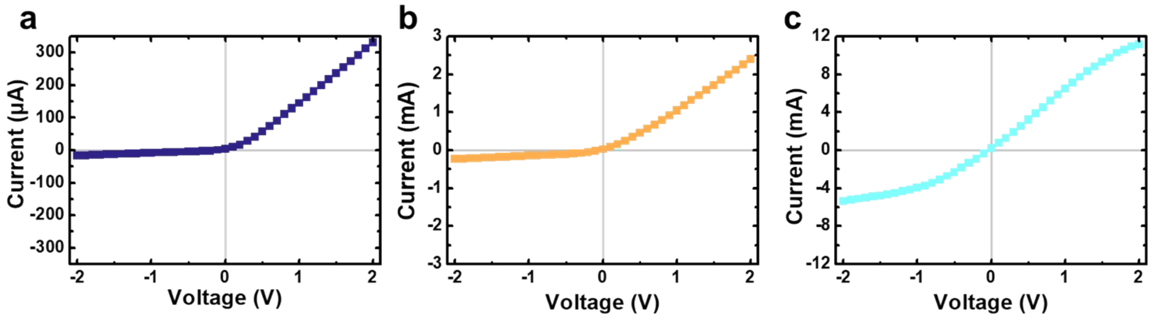

Fig. S5. Illustrated experimental I-V curves of the Nafion/ANM recorded in (a) 10 mM, (b) 100 mM and (c) 500 mM KCl solutions.

Table S1. The ICR ratio of Nafion/ANM as a function of the KCl concentration.

	KCl concentration (mM)			
	1	10	100	500
Rectification ratio	15.1±2.5	18.2±4.3	10.3±0.7	2.0±0.3

Table S2. The ICR ratio of Nafion/ANM as a function of the ANM thickness.

	ANM thickness (μm)			
	15.0	38.8	62.2	85.7
Rectification ratio	10.3±1.2	18.2±4.3	12.4±3.0	2.9±0.1

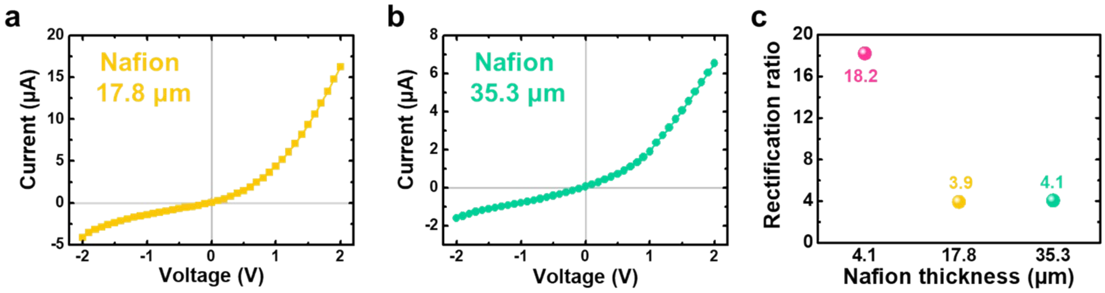

Fig. S6. (a,b) I-V curves of the Nafion/ANM with various Nafion thicknesses recorded in 10 mM KCl solution: (a) ~17.8 μm, and (b) ~35.3 μm. (c) Calculated ICR ratio as a function of the Nafion thickness.

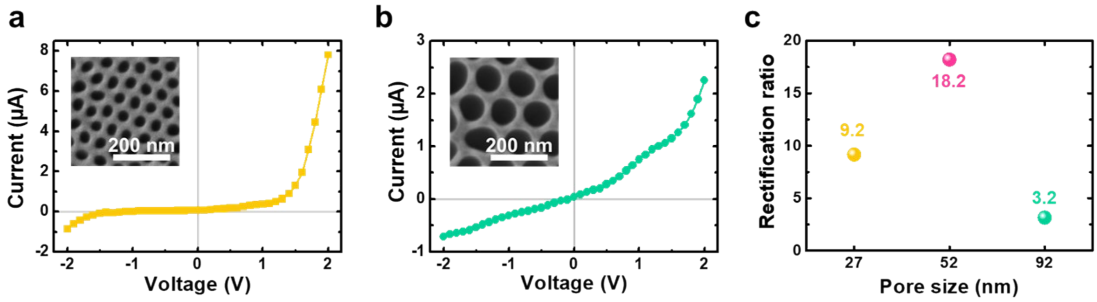

Fig. S7. (a,b) I-V curves of the Nafion/ANM with various pore sizes of ANM recorded in 10 mM KCl solution: (a) ~27 nm, and (b) ~92 nm. Insets depict the top-view SEM images of the other two ANMs used in the measurements. (c) Calculated ICR ratio as a function of the ANM pore size.

Theoretical model

Ion transport property and osmotic energy conversion in the Nafion/ANM system (Fig. S8) considered can be described by the coupled Poisson-Nernst-Planck and Stokes-Brinkman equations with considering the space charge nature originating from the Nafion layer,[1-3]

$$-\nabla^2\phi = \frac{\sum_{i=1}^{2} F z_i C_i + \Phi\rho_{\mathrm{PE}}}{\varepsilon_f} \tag{S1}$$

$$\nabla\cdot\mathbf{N}_i = \nabla\cdot\left(\mathbf{u}C_i - D_i\nabla C_i - \frac{F z_i C_i D_i}{RT}\nabla\phi\right) = 0,\ i = 1, 2 \tag{S2}$$

$$\mu\nabla^2\mathbf{u} - \nabla p - \nabla\phi\left(\sum_{i=1}^{2} F z_i C_i\right) - \Phi\frac{\mu}{(\lambda_{PE})^2}\mathbf{u} = \mathbf{0} \tag{S3}$$

$$\nabla\cdot\mathbf{u} = 0 \tag{S4}$$

In the above, ρ_{PE} is the space charge density of the Nafion layer; ϕ, F, and R are the electrical potential, Faraday constant, and gas constant, respectively; ε_f, $\mathbf{u}$, p, T, and μ are the permittivity, velocity, pressure, temperature and dynamic viscosity of fluid, respectively; z_i, C_i, and D_i are the valence, concentration, flux, and diffusivity of the ionic species of i ($i = 1$ for cations and $i = 2$ for anions); Φ is the region function ($\Phi = 1$ represents the region inside the Nafion layer and $\Phi = 0$ represents the region outside the Nafion layer); λ_{PE} is the softness degree of Nafion layer and we assumed $\lambda_{PE} = 1$ nm, consistent with the value of artificial polyelectrolytes (*ca.* 0.1-10 nm).

We assumed the following boundary conditions. (i) The end of the reservoir outside the Nafion layer is applied at a voltage bias V ($\phi = V$), while the end of the other reservoir is grounded ($\phi = 0$). (ii) The ionic concentrations at the ends of two reservoirs reach the bulk values of electrolyte concentration and no external pressure gradient is applied through the system ($p = 0$). (iii) The rigid walls of the ANM are non-slip ($\mathbf{u} = 0$), ion-impenetrable ($\mathbf{n}\cdot\mathbf{N}_i = 0$), and carry a fixed surface charge density of σ_s ($-\varepsilon_f \mathbf{n}\cdot\nabla\phi=\sigma_s$). Here $\mathbf{n}$ is the unit outer normal vector. (iv) The rigid walls at the upper and lower membrane interfaces are non-slip ($\mathbf{u}=0$), ion-impenetrable ($\mathbf{n}\cdot\mathbf{N}_i=0$), and uncharged ($\mathbf{n}\cdot\nabla\phi=0$). (v) All the electric potential, electric field, ionic concentrations, and flow field are continuous at the Nafion/liquid interfaces. (vi) The symmetric boundary condition is specified along the axis of the Nafion/ANM system.

The ionic current through the system can be calculated by the following equation,

$$I=\int_S\left(\sum_{i=1}^{2}Fz_i\mathbf{N}_i\right)\cdot\mathbf{n}dS\,, \tag{S5}$$

where S denotes either end of the two reservoirs. The other parameters used in the modeling include $\rho_{PE}=-5\times10^7\ \mathrm{C/m^3}$ and $\sigma_s=0.08\ \mathrm{C/m^2}$.

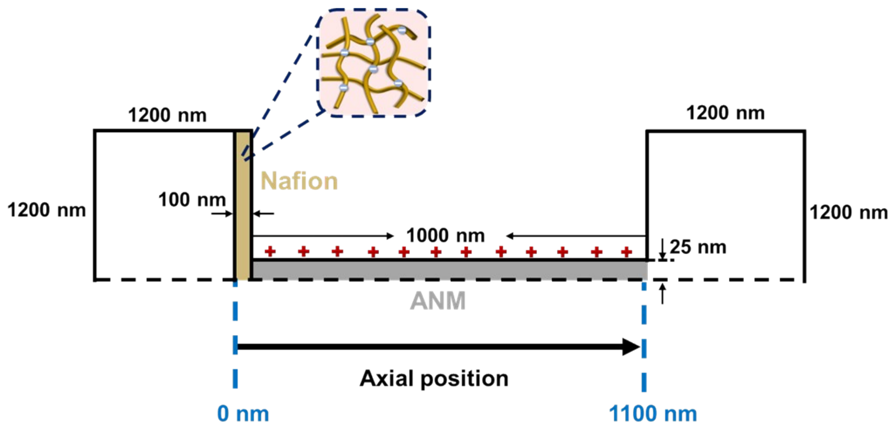

Fig. S8. Schematic of the simulated Nafion/ANM system (not to scale). The Nafion thin film is considered as a negatively charged polyelectrolyte layer carrying a space charge density of -5×10^7 C/m^3.

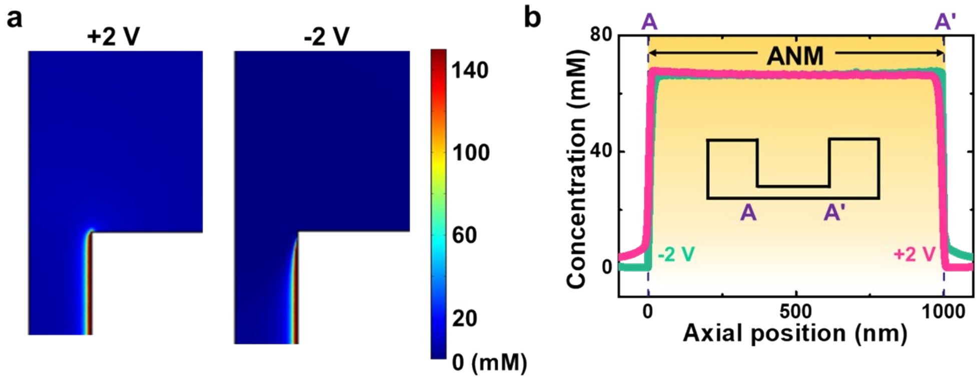

Fig. S9. (a) Spatial and (b) axial variations of the total ion concentration (K^+ and Cl^-) in the symmetric ANM at the two transmembrane voltages of +2 V and −2 V at 10 mM KCl. The surface charge density on the ANM wall is assumed to be 0.08 C/m^2.

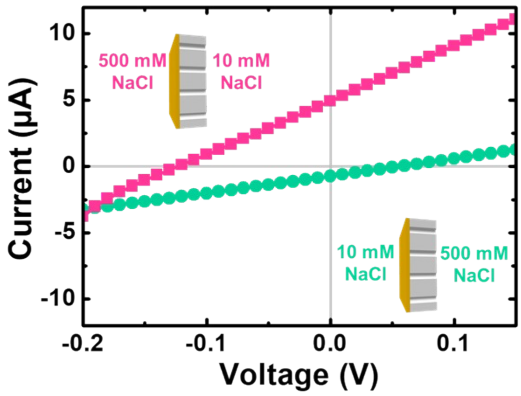

Fig. S10. I-V curves of the Nafion/ANM under two opposite directions of a 50-fold NaCl gradient. When the Nafion side is in contact with a higher-concentration solution (pink squares), the measured open-circuit voltage (V_{oc}) and closed-circuit current (I_{sc}) are *ca.* 121 mV and 4.84 μA, respectively, both of which are significantly higher than the values (*i.e.*, 59.6 mV and 0.77 μA) at the opposite concentration gradient (green circles). This indicates that higher ion selectivity and faster ion transport can be realized when the Nafion side of heterogeneous membrane faces the higher-concentration solution.

Electrode calibration

Referring to the equivalent circuit diagram shown in Fig. S11, the measured open-circuit voltage (V_{oc}), when a salinity gradient is applied through the Nafion/ANM, consists of two parts including the osmotic potential (V_{osm}) and the redox potential (V_{red}) that originates from the uneven potential drop at two electrodes in the presence of a salinity gradient, which satisfy the following equation,

$$V_{oc} = V_{\mathrm{red}} + V_{\mathrm{osm}} \tag{S6}$$

To estimate the pure salinity gradient-driven V_{osm} and osmotic current (I_{osm}), the electrode calibration with V_{red} should be made, for which the current-voltage curves were recorded by applying the sweeping voltages varying from −0.2 V to 0.2 V with a step of 0.01 V in the presence and absence of the Nafion/ANM. If no Nafion/ANM, the measured voltage was identified as the V_{red}. The obtained values of V_{red} are 46.7, 58.6, and 78.3 mV under 50-, 100-, and 500-fold NaCl gradients, respectively, as shown in Table S3.

Evaluation of cation selectivity

The cation selectivity of the Nafion/ANM can be estimated by calculation of the cation transference number (t^+) according to the following equation,

$$t^+ = \frac{V_{\mathrm{osm}}}{2\left(\frac{RT}{F}\right)\ln\left(\frac{\gamma_{\mathrm{H}} C_{\mathrm{H}}}{\gamma_{\mathrm{L}} C_{\mathrm{L}}}\right)} + 0.5 \tag{S7}$$

where γ is the activity coefficient of salt solutions and the subscripts, H and L, denote the properties of salt solutions in high- and low-concentration reservoirs, respectively. In general, t^+=0.5 represents the non-ion-selective pore membrane and t^+=1 represents the ideally cation-selective membrane.

Evaluation of energy conversion efficiency

Then the maximum osmotic energy conversion efficiency ($\eta_{\max}$) of the Nafion/ANM can be calculated by

$$\eta_{max} = \frac{(2t^{+} - 1)^2}{2} \times 100\% \qquad \text{(S8)}$$

The values of V_{osm}, I_{osm}, t^{+} and η_{max} of the Nafion/ANM tested under various NaCl gradients were summarized in Table S3.

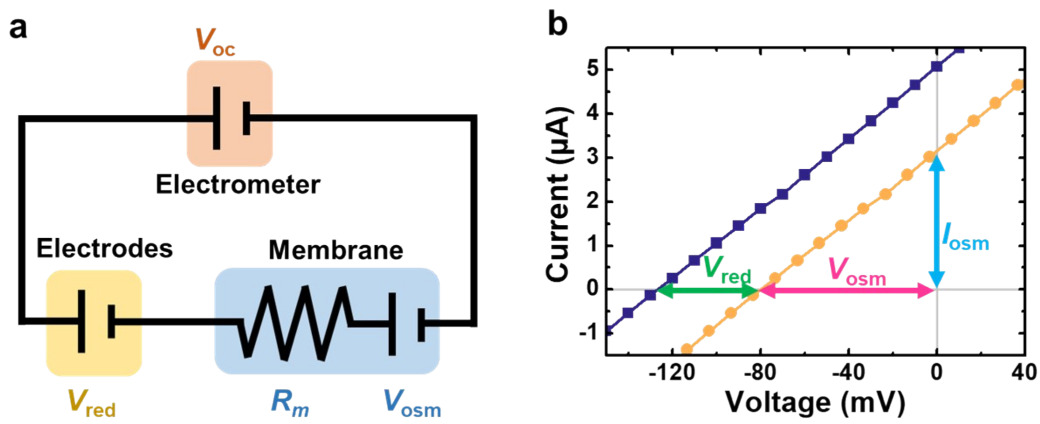

Fig. S11. (a) Schematic illustrating the equivalent circuit diagram of the considered osmotic energy conversion system. The measured open-circuit voltage (V_{oc}) includes two parts: redox potential (V_{red}) at the electrodes and the pure salinity gradient-driven osmotic potential (V_{osm}). Only the V_{osm} is contributed from the ion-selective membrane subjected to a salinity gradient. R_m is the electrical resistance of the membrane. (b) Illustrated I-V curves of the Nafion/ANM under a 50-fold NaCl gradient (0.5 M/0.01 M) before (squares with line) and after (spheres with line) the redox potential calibration. The V_{osm} and osmotic current (I_{osm}) can be directly read from the intercepts on the voltage and current axes of the calibrated curve, respectively.

Table S3. Osmotic power conversion performances tested under various NaCl gradients.

Nafion/ANM	Fixed low concentration at 0.01 M		
	50-fold NaCl	100-fold NaCl	500-fold NaCl
V_{oc} (mV)	125	134	159
V_{red} (mV)	46.7	58.6	78.3
V_{osm} (mV)	78.3	75.4	80.7
I_{sc} (μA)	5.01	7.13	15.3
I_{osm} (μA)	3.04	3.64	7.54
t^{+}	0.933	0.855	0.783
η_{max} (%)	37.5	25.3	16.0

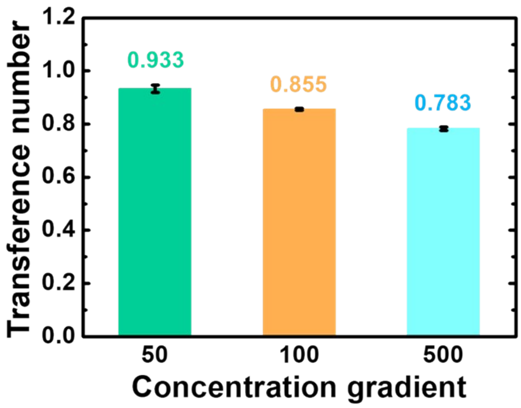

Fig. S12. Cation transference number (t^+) of the Nafion/ANM tested at various NaCl gradients. The t^+ values under 50-, 100-, and 500-fold concentration gradients are *ca.* 0.933, 0.855, and 0.783, respectively.

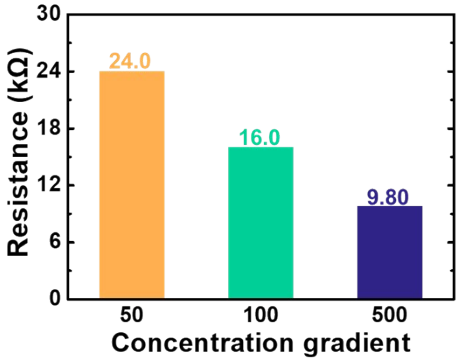

Fig. S13. The external resistance at which the Nafion/ANM can achieve the maximum power output.

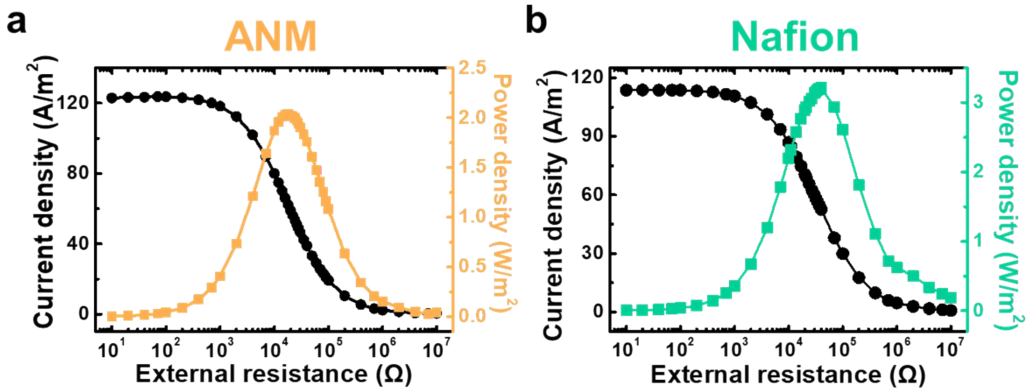

Fig. S14. The osmotic power conversion performance generated by (a) the ANM and (b) pure Nafion membrane in 0.5 M/0.01 M NaCl gradient. The averaged maximum power densities achieved by the ANM and pure Nafion membrane are *ca.* 2.04 and 3.18 W/m^2, respectively.

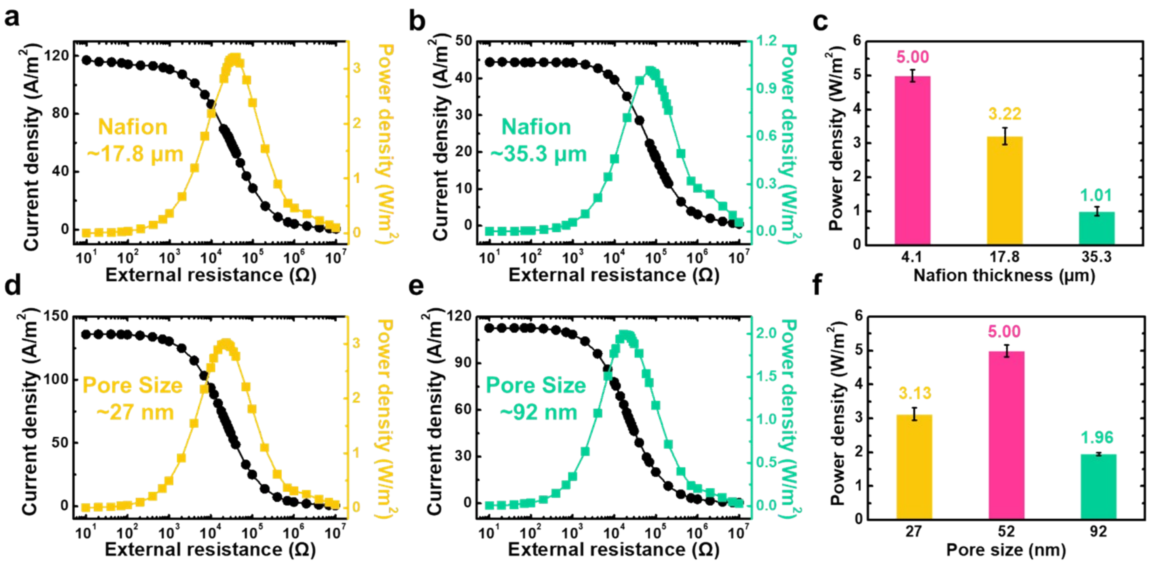

Fig. S15. (a-c) Effect of the Nafion thickness on the osmotic power conversion performance of the Nafion/ANM with a Nafion thickness of (a) ~17.8 μm and (b) ~35.3 μm in 0.5 M/0.01 M NaCl gradient. (c) The achieved power density as a function of the Nafion thickness. (d-e) Effect of the pore size of ANM on the osmotic power conversion performance of the hybrid Nafion/ANM by using an ANM with pore diameter of about (d) 27 nm and (e) 92 nm in 0.5 M/0.01 M NaCl gradient. (f) The achieved power density as a function of the ANM pore size.

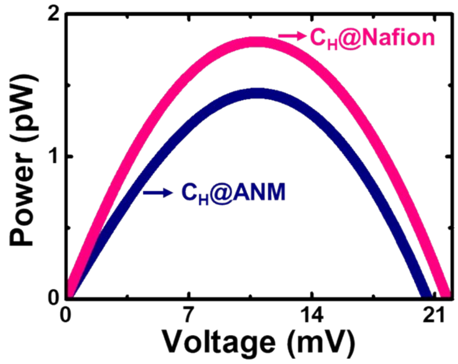

Fig. S16. Simulated P-V curves for the Nafion/ANM under two configurations of a 500-fold salinity gradient. Pink (blue) curve indicates that the higher concentration is set at the Nafion (ANM) side.

Table S4. Comparison of the osmotic energy conversion efficiency and power density achieved by the present Nafion/ANM and the state-of-the-art ion-selective membranes reported in the literatures at the same 0.5 M/0.01 M NaCl gradient.

Membrane	**Efficiency (%)**	P_{max} **(W/m²)**	**Reference**
PVMs	-	4.1	4
UiO-66-NH_2@ANM	-	2.96	5
SPEEK/AAO	-	4.8	6
BCP/AAO	-	2.94	7
PSS/MOF/AAO	-	2.87	8
MesoC/AAO	37.3	3.46	9
SNF/AAO	17.2	2.86	10
PES-Py/PAEK-HS	35.7	2.66	11
MXene/Kevlar	35.0	3.7	12
GO/SNF/GO	27.2	5.07	13
MoS_2/CNF	32.0	5.2	14
Nafion/ANM	37.5	5.13	This work

Table S5. Comparison of the power density outputted by the present Nafion/ANM and the reported ion-selective membrane in hypersaline environment (5 M/0.01 M NaCl gradient).

Membrane	**Thickness (μm)**	P_{max} **(W/m²)**	**Reference**
PES-Py/PAEK-HS	21.0	5.1	11
GO/SNF/GO	10.7	16.2	13
MoS_2/CNF	4.0	15.6	14
GO/CNFs	9.0	13.3	15
CS/SA	30	19.4	16
MXene/PS-*b*-P2VP	1.2	12.4	17
SPEEK	27.0	20.2	18
HEMAP	24.0	19.6	19
SF	0.1	21.7	20
SPEEK/AAO	80	12.5	6
Nafion/ANM	21.6	22.1	This work

References

1. L. H. Yeh, M. Zhang, S. Qian, J. P. Hsu and S. Tseng, *J. Phys. Chem. C*, 2012, **116**, 8672-8677.
2. C. Y. Lin, J. P. Hsu and L. H. Yeh, *Sens. Actuator B-Chem.*, 2018, **258**, 1223-1229.
3. Z. Zeng, Y. Ai and S. Qian, *Phys. Chem. Chem. Phys.*, 2014, **16**, 2465-2474.
4. L. Cao, H. Wu, C. Y. Fan, Z. M. Zhang, B. B. Shi, P. F. Yang, M. Qiu, N. A. Khan and Z. Y. Jiang, *J. Mater. Chem. A*, 2021, **9**, 14576-14581.
5. Y. C. Liu, L. H. Yeh, M. J. Zheng and K. C. W. Wu, *Sci. Adv.*, 2021, **7**, eabe9924.
6. S. H. Hou, Q. R. Zhang, Z. Zhang, X. Y. Kong, B. Z. Lu, L. P. Wen and L. Jiang, *Nano Energy*, 2021, **79**, 105509.
7. X. Sui, Z. Zhang, C. Li, L. C. Gao, Y. Zhao, L. J. Yang, L. P. Wen and L. Jiang, *ACS Appl. Mater. Interfaces*, 2019, **11**, 23815-23821.
8. R. R. Li, J. Q. Jiang, Q. Q. Liu, Z. Q. Xie and J. Zhai, *Nano Energy*, 2018, **53**, 643-649.
9. J. Gao, W. Guo, D. Feng, H. T. Wang, D. Y. Zhao and L. Jiang, *J. Am. Chem. Soc.*, 2014, **136**, 12265-12272.
10. W. W. Xin, Z. Zhang, X. D. Huang, Y. H. Hu, T. Zhou, C. C. Zhu, X. Y. Kong, L. Jiang and L. P. Wen, *Nat. Commun.*, 2019, **10**, 3876.
11. X. B. Zhu, J. R. Hao, B. Bao, Y. H. Zhou, H. B. Zhang, J. H. Pang, Z. H. Jiang and L. Jiang, *Sci. Adv.*, 2018, **4**, eaau1665.
12. Z. Zhang, S. Yang, P. P. Zhang, J. Zhang, G. B. Chen and X. L. Feng, *Nat. Commun.*, 2019, **10**, 2920.
13. W. W. Xin, H. Y. Xiao, X. Y. Kong, J. J. Chen, L. S. Yang, B. Niu, Y. C. Qian, Y. F. Teng, L. Jiang and L. P. Wen, *ACS Nano*, 2020, **14**, 9701-9710.
14. C. C. Zhu, P. Liu, B. Niu, Y. N. Liu, W. W. Xin, W. P. Chen, X. Y. Kong, Z. Zhang, L. Jiang and L. P. Wen, *J. Am. Chem. Soc.*, 2021, **143**, 1932-1940.
15. Y. D. Wu, W. W. Xin, X. Y. Kong, J. J. Chen, Y. C. Qian, Y. Sun, X. L. Zhao, W. P. Chen, L. Jiang and L. P. Wen, *Materials Horizons*, 2020, **7**, 2702-2709.
16. G. S. Bian, N. Pan, Z. H. Luan, X. Sui, W. X. Fan, Y. Z. Xia, K. Y. Sui and L. Jiang, *Angew. Chem.-Int. Edit.*, 2021, **60**, 20294-20300.
17. X. Lin, P. Liu, W. Xin, Y. Teng, J. Chen, Y. Wu, Y. Zhao, X. Y. Kong, L. Jiang and L. P. Wen, *Adv. Funct. Mater.*, 2021, **31**, 2105013.
18. Y. Y. Zhao, J. Wang, X. Y. Kong, W. W. Xin, T. Zhou, Y. C. Qian, L. S. Yang, J. H. Pang, L. Jiang and L. P. Wen, *Natl. Sci. Rev.*, 2020, **7**, 1349-1359.
19. W. P. Chen, Q. Wang, J. J. Chen, Q. R.

Zhang, X. L. Zhao, Y. C. Qian, C. C. Zhu, L. S. Yang, Y. Y. Zhao, X. Y. Kong, B. Z. Lu, L. Jiang and L. P. Wen, *Nano Lett.*, 2020, **20**, 5705-5713.

20. J. J. Chen, W. W. Xin, X. Y. Kong, Y. C. Qian, X. L. Zhao, W. P. Chen, Y. Sun, Y. D. Wu, L. Jian and L. P. Wen, *ACS Energy Lett.*, 2020, **5**, 742-748.